








# SOLEIL: single-objective lens inclined light sheet localization microscopy

SHIH-TE HUNG,<sup>1</sup> JELMER CNOSSEN,<sup>1</sup> DANIEL FAN,<sup>1</sup> MARIJN SIEMONS,<sup>2</sup>  DAPHNE JURRIENS,<sup>2</sup> KRISTIN GRUBMAYER,<sup>3</sup>  OLEG SOLOVIEV,<sup>1,4</sup>  LUKAS C. KAPITEIN,<sup>2</sup>  AND CARLAS S. SMITH<sup>1,5,\*</sup> 

<sup>1</sup>*Delft Center for Systems and Control, Delft University of Technology, Delft, Netherlands*

<sup>2</sup>*Cell Biology, Neurobiology and Biophysics, Department of Biology, Faculty of Science, Utrecht University, Utrecht, Netherlands*

<sup>3</sup>*Department of Bionanoscience and Kavli Institute of Nanoscience Delft, Delft University of Technology, Delft, Netherlands*

<sup>4</sup>*Flexible Optical B.V., Polakweg 10-11, 2288 GG Rijswijk, Netherlands*

<sup>5</sup>*Department of Imaging Physics, Delft University of Technology, Delft, Netherlands*

\**C.S.Smith@tudelft.nl*

**Abstract:** High-NA light sheet illumination can improve the resolution of single-molecule localization microscopy (SMLM) by reducing the background fluorescence. These approaches currently require custom-made sample holders or additional specialized objectives, which makes the sample mounting or the optical system complex and therefore reduces the usability of these approaches. Here, we developed a single-objective lens-inclined light sheet microscope (SOLEIL) that is capable of 2D and 3D SMLM in thick samples. SOLEIL combines oblique illumination with point spread function PSF engineering to enable dSTORM imaging in a wide variety of samples. SOLEIL is compatible with standard sample holders and off-the-shelf optics and standard high NA objectives. To accomplish optimal optical sectioning we show that there is an ideal oblique angle and sheet thickness. Furthermore, to show what optical sectioning delivers for SMLM we benchmark SOLEIL against widefield and HILO microscopy with several biological samples. SOLEIL delivers in 15  $\mu\text{m}$  thick Caco2-BBE cells a 374% higher intensity to background ratio and a 54% improvement in the estimated CRLB compared to widefield illumination, and a 184% higher intensity to background ratio and a 20% improvement in the estimated CRLB compared to HILO illumination.

© 2022 Optica Publishing Group under the terms of the [Optica Open Access Publishing Agreement](#)

## 1. Introduction

Single-molecule localization microscopy (SMLM) has been shown to surpass the diffraction limit and has become an important imaging technology for biological research [1–6]. SMLM overcomes the diffraction limit by localizing sparsely activated single molecules. The ultimate resolution of an SMLM reconstruction is limited not by the optical resolution, but by the localization uncertainty and the localization density of the single molecules [7]. The theoretical minimum localization uncertainty can be calculated using the Cramér-Rao lower bound (CRLB) [6,8]. The CRLB predicts that an increase in background photon counts increases the localization uncertainty [6]. An increase in localization uncertainty leads to a decrease in the theoretical maximum detection efficiency [9]. The reduction in detection efficiency reduces the number of detected molecules and therefore the localization density. Therefore, an increase in background photon counts leads to a deterioration of the ultimate resolution in localization microscopy.

In biological samples, the main sources of background fluorescence are auto-fluorescence and fluorescence from excited out-of-focus dyes [10–17]. A common strategy to reduce background fluorescence is increasing the optical sectioning capabilities of the microscope. For example,

total internal reflection microscopy (TIRF) increases the optical sectioning by illuminating the coverslip with a super-critical angle and the sample with an evanescent field. This evanescent field ( $e^{-1}$  at  $\approx 200$  nm) limits the axial excitation range above the coverslip and therefore reduces background fluorescence [18,19].

Highly inclined and laminated optical sheet (HILO) microscopy and variable-angle epifluorescence (VAEM) microscopy extend the axial excitation range, by illuminating the coverslip at a sub-critical angle and the sample with a tilted beam [20,21]. Similar to TIRF microscopy this approach typically requires a total internal reflection-compatible objective lens ( $NA \geq 1.45$ ) to achieve optimal performance. The optical sectioning of HILO and VAEM is proportional to the field of view (FOV). HILO microscopy has been demonstrated on SMLM with DNA-PAINT [22]. To accomplish sufficient background-reduction, the field of view (FOV) in both dimensions is usually limited to 5 to 10  $\mu m$ . Furthermore, HILO is typically limited to thin specimens due to aberration, originating from the index-mismatch between oil and the sample of interest [23]. The trade-off between the size of the field of view and the thickness of optical sectioning has been abated by highly inclined swept tile (HIST) microscopy [24]. HIST microscopy sweeps an elongated HILO beam and synchronizes the excitation area with the active pixel of the camera to extend the FOV while maintaining the optical sectioning capabilities of HILO.

A way to further optimize optical sectioning is by the use of light sheet microscopy. Light sheet microscopy is also called selective plane illumination microscopy (SPIM). Light sheet microscopy is typically accomplished using an objective for the detection of the fluorescence signal and an additional objective for illuminating the sample with a thin sheet of light [25,26]. The orthogonal dual objective lens configuration hinders the use of high NA detection objectives. To extend the FOV beyond the size predicted by Gaussian beam optics, axially swept light sheet microscopy (ASLM) sweeps the light sheet axially and synchronizes the light sheet excitation with the camera readout [27,28]. While this approach allows for a larger FOV size, the drawback is that a lot of signal is lost, as only a thin line on the detector is read out. However, the acquisition speed of ASLM is slower than with a static light sheet because of the nature of the scanning/sweeping strategy. Tilted light sheet microscopy (TILT3D) and lateral interference tilted excitation microscope (LITE) successfully addressed the problem of a low detection NA by use of a tilted (non-orthogonal) illumination configuration [29,30]. At the cost of detection NA, this can be further extended to dual tilted illumination [31]. TILT3D employs PSF engineering making it suitable for 3D SMLM [29]. The major disadvantages of these multi-objective approaches are that the microscope alignment and assembly are complex and that it often requires a custom-made sample holder.

Single objective light sheet microscopes (soSPIM) have been developed in an attempt to reduce the complexity of multi-objective light sheet microscopes [32–34]. soSPIMs makes use of special sample holders to rotate the light sheet by  $90^\circ$ . This operation aligns the light sheet with the focal plane and thereby creates an in-focus light sheet without the use of additional objectives. These custom sample holders are made with special nano-fabrication techniques. The complexity of the fabrication, sample mounting, and alignment of these customized sample holders significantly increases the experiment complexity.

To alleviate the disadvantage of both the sample mounting and low detection and illumination NA, oblique plane microscopes (OPM) have been developed [35–40]. OPM is related to HILO and VAEM as they all utilize inclined illumination. However, to optimize the FOV and the optical sectioning OPM uses a significantly different illumination scheme that makes use of the principles from light sheet microscopy [24,41]. The combination of oblique illumination and detection avoids, in principle, the use of custom-made sample holders. OPM has fewer constraints in terms of sample preparation, and its development followed that of conventional two-objective light sheet microscopy, with extensions such as multi-color [42], multi-view imaging [43], and also has the benefits of remote lateral [37,44,45] and axial scanning [46] of the light sheet and detection



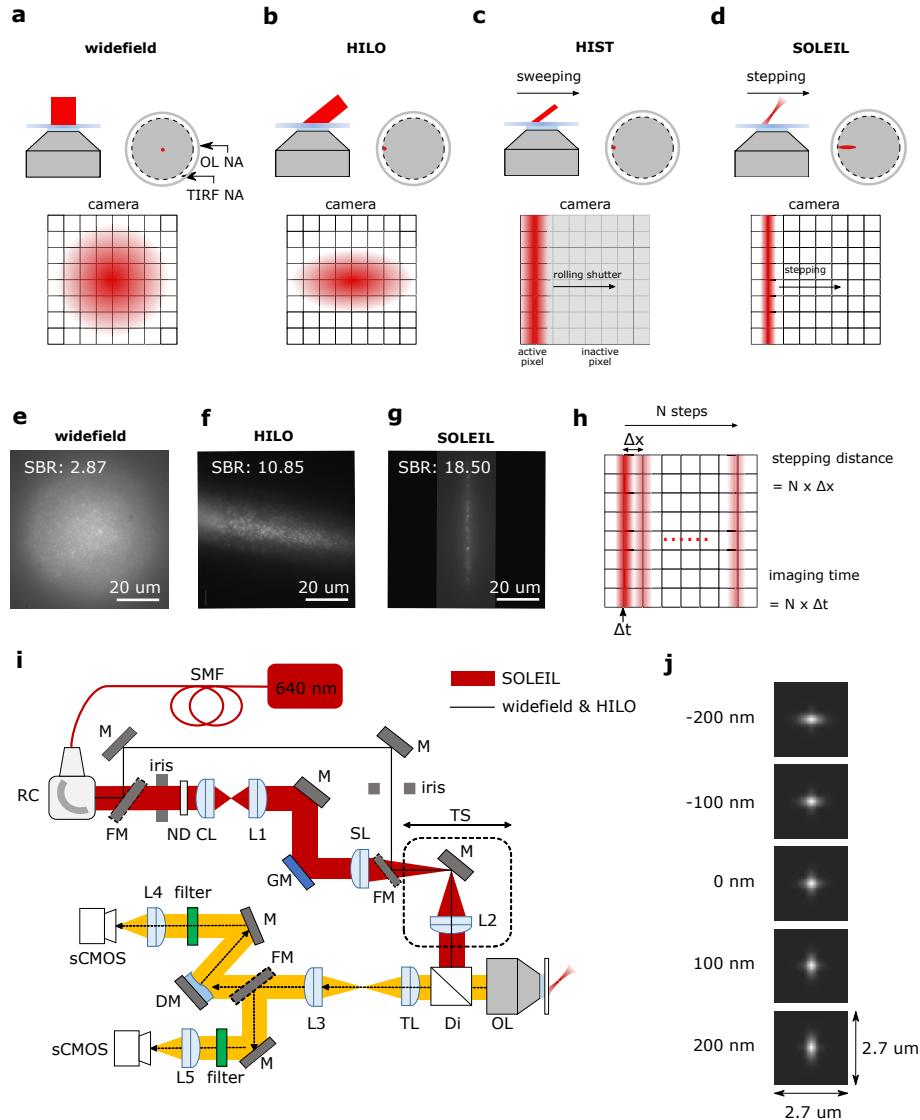


**Fig. 1.** Introduction of SOLEIL and the benchmark between the different illumination modalities in terms of the signal-to-background-ratio (SBR). (a-d) upper row: Illumination profile of the different illumination schemes (widefield, HILO, HIST, and proposed method SOLEIL) and corresponding back focal planes (red). lower row: camera view of each illumination scheme. The details about HILO, HIST, SOLEIL are in section 2.3. (e-g) the raw images acquired from 23 nm fluorescence beads embedded in 1 % agarose gel (see section 2.10.1) with corresponding SBR (see section 2.6). (h) stepping procedure, where the total stepped distance is the step size ( $\Delta x$ ) times the number of steps ( $N$ ). The imaging time for the whole FOV is the exposure time per step ( $\Delta t$ ) times the number of steps. (i) Schematic representation of the optical system of SOLEIL. SMF, single-mode fiber; RC, reflective collimator; ND, neutral density filter; CL, cylindrical lens; L, lens; GM, galvo mirror; SL, scan lens; TS, translation stage; Di, dichroic mirror; TL, tube lens; OL, objective lens; DM, deformable mirror; filter, emission filter; FM, flip mirror; M, reflective mirror. Details of the optical elements are presented in the method section. (j) Simulation of the astigmatism aberration engineered PSF.

planes. The oblique detection is often made possible through the use of two additional objective lenses that are placed downstream in the emission path. These two objectives make it possible to re-position the focal plane to match the oblique light sheet illumination. A disadvantage of these approaches was a truncated detection NA [40], which deteriorated the resolution and the quality of the point spread function (PSF). This weak point has recently been addressed with custom-made objective lenses making it possible to use them close to the maximum detection NA (1.27) and improve the quality of the PSF [39,47]. However, the use of two additional objectives significantly increases the complexity of the system and more importantly decreases the photon throughput. Objective lenses have a transmission of about 80% (see specifications), which results in 35% reduction of photon throughput.

Here, we present SOLEIL (Single-Objective Lens Inclined light sheet), a platform that combines principles of PSF engineering and oblique plane microscopy to provide an alternative solution to alleviate the previously discussed disadvantages of existing HILO and high-NA light sheet approaches for SMLM. We show that oblique plane microscopy has an optimal illumination angle and sheet thickness to achieve the best possible optical sectioning. We have determined the NA and inclined angle for the best optical sectioning using OPM, which results in a light sheet width of  $0.645 \mu\text{m}$  and length of  $66 \mu\text{m}$  on the camera (Fig. 3 (c)). To acquire large FOVs the light sheet needs to be translated (Fig. 1 (d)). To experimentally compare the performance of optical sectioning of SOLEIL with widefield and HILO microscopy, we designed a microscope that can switch between the different illumination schemes (widefield, HILO, and SOLEIL). To quantify the difference in optical sectioning performance between widefield, HILO, and SOLEIL microscopy we imaged fluorescent beads embedded in agarose gel (see section 2.10.1) and measured the signal-to-background ratio Fig. 1 (e-g). To demonstrate the impact of SOLEIL for SMLM we benchmarked it against widefield and HILO microscopy on dSTORM samples. We show that in several biological samples SOLEIL achieves a significant improvement in the estimated CRLB.

## 2. Method

### 2.1. Optical system

An overview of the SOLEIL microscope is shown in Fig. 1(e). The sample was placed on a stick-slip piezo stage (Smartact; x,y an SLC1730; z an SLC1720). The light sheet was generated using a doublet achromatic cylindrical lens (CL, Thorlabs, ACY254-250-B). One achromatic doublet lens (L1, Thorlabs, AC254-300-A-ML) was assembled with the CL as a 4f-telescope. A galvo mirror (Scanlab, dynAXIS 20 mm) was placed at the pupil plane of the scan lens (SL, TTL200MP, Thorlabs) forming a scanning module for translating the light sheet. The doublet achromatic lens (L2, Thorlabs, AC254-200-A-ML) and the reflective mirror (M, Thorlabs, BB1-E02) were mounted on a translation stage (TS, Thorlabs, XR25P/M) to shift the spot at the pupil plane generating the excitation light sheet. The dichroic mirror (Semrock, Di03-R405/488/561/635-t1-25x36) was used to separate the excitation and emission path. The 180 mm focal length tube lens (Olympus, SWTLU-C) is combined with a 60 times objective lens (Olympus, UPlanSAPO 60x Oil NA 1.35). In the emission path, an achromatic lens (L3, AC254-200-A-ML) was assembled as a 4f-telescope with the TL, which conjugated the back focal plane of the objective lens to the deformable mirror (Alpao DM69-15). The deformable mirror is used to modify the pupil phase in the emission path, to enable PSF engineering needed for 3D SMLM. The deformable mirror was rotated by approximately  $15^\circ$  to reflect the emission light to the sCMOS camera (Andor Zyla 4.2). An emission filter (AHF, FF01-446/510/581/703-25) was used to block the back-reflected excitation laser. The achromatic lens (L4, AC254-200-A-ML) images the pupil plane at the deformable mirror to the sCMOS camera. A flip mirror was used to switch the emission path to bypass the deformable mirror, which was used for 2D

localization microscopy. The sCMOS camera and galvo mirror were synchronized using an Arduino micro-controller. The sCMOS camera acquired an image at each galvo mirror step.

To achieve widefield and HILO illumination, we used a flip mirror to bypass the optical path that generates the light sheet. To adjust the HILO illumination an iris and a translation stage (TS) were used to adjust the spot size and the HILO angle (see Fig. 1 (i)).

## 2.2. Optimized optical sectioning for SOLEIL microscopy

To find the configuration that can achieve the optimal optical sectioning with SOLEIL microscopy, we simulated the excitation profile with varying NA and determined the resulting optical sectioning from the simulated data. We modelled the excitation ( $\lambda = 640$  nm) profile as an inclined Gaussian beam (supplementary section 1). The waist of Gaussian beam  $w_0$  and the inclined angle of the Gaussian beam ( $\theta_{\text{inc}}$ ) were corrected for the refraction from the layer between the coverslip/immersion oil ( $n = 1.52$ ) and the dSTORM buffer ( $n = 1.33$ ). The simulation window ranged from  $-5$  to  $5$   $\mu\text{m}$  along the optical axis ( $z$ ) from the imaging plane and across the FOV ( $x$ ) (Fig.S1).

We defined the optical sectioning as the (projected) thickness of the beam at which the intensity drops to  $e^{-1}$  along the optical axis (Fig. 2), which matches with the definition of the penetration depth of TIRF illumination [48,49]. To determine the thickness of the optical sectioning, we extracted the intensity profile of simulated Gaussian beam along the  $z$ -axis (white dashed line in Fig. 2 (a)) and fitted it to a Gaussian function with the parameters of amplitude, center, and width of Gaussian function ( $\sigma$ ) by minimizing the mean square error Fig. 2 (b). The  $2\sqrt{2}$  times of estimated  $\sigma$  of Gaussian function was the thickness of optical sectioning.

We found that a higher illumination NA generates a thinner Gaussian beam at the cost of reducing the (maximum) possible inclined angle ( $\theta_{\text{inc}}$ ) Fig. 2 (c). Both the illumination NA and the inclined angle have an impact on the optical sectioning Fig. 2 (c,d). The best optical sectioning of SOLEIL microscopy is achieved with an illumination NA of 0.66 and an inclined angle of  $38^\circ$  from the optical axis of the objective lens Fig. 2(e). At this optimal NA, the width is  $0.645$   $\mu\text{m}$  and the length of  $66$   $\mu\text{m}$ . The stepping speed is limited, because the microscope can only acquire photons from the single-molecule when the single-molecule is in its fluorescent on-state and it is illuminated.

## 2.3. Comparative analysis between HILO, HIST, and SOLEIL microscopy

To achieve optical sectioning in HILO, HIST, and SOLEIL microscopy different optical configurations are used. In the Fig. 3 (a-c), we show a schematic of HILO, HIST, and SOLEIL microscopy. HILO microscopy (Fig. 3 (a)) adopts an inclined (collimated) excitation beam to generate the optical sectioning. The excitation beam illuminated the sample under an angle and therefore a projected beam width is observed on the camera ( $R_{1,\text{HILO}} > R_{2,\text{HILO}}$ ). In HILO microscopy, increasing the excitation area increases the thickness of optical sectioning (see supplementary section 3). This typically limits the usability of HILO microscopy. HIST microscopy is an improved version of HILO microscopy, and it adopts a pair of cylindrical lenses to elongate the beam in one dimension ( $R_{1,\text{HIST}} < R_{2,\text{HIST}}$ ) (Fig. 3 (b)). Furthermore, the excitation area is swept over the sample by a galvo mirror and the pixel readout of camera is synchronized with the excitation area (i.e. the area that is illuminated at a single galvo position). With the above two modifications, HIST microscopy acquires a larger FOV (i.e. the area acquired from multiple galvo positions) compared to HILO microscopy without increasing the thickness of optical sectioning. With SOLEIL, we adopt an inclined light sheet to generate the optical sectioning (Fig. 3 (c)), which is different from HILO and HIST microscopy. This is accomplished by moving a lens to place the beam at the edge of the back focal plane of the objective to generate the light sheet at an inclined angle. With SOLEIL, similar to HIST, the light sheet is stepped over the sample by a galvo mirror to image the desired FOV (Fig.1 (d)). The light sheet is not scanned but is

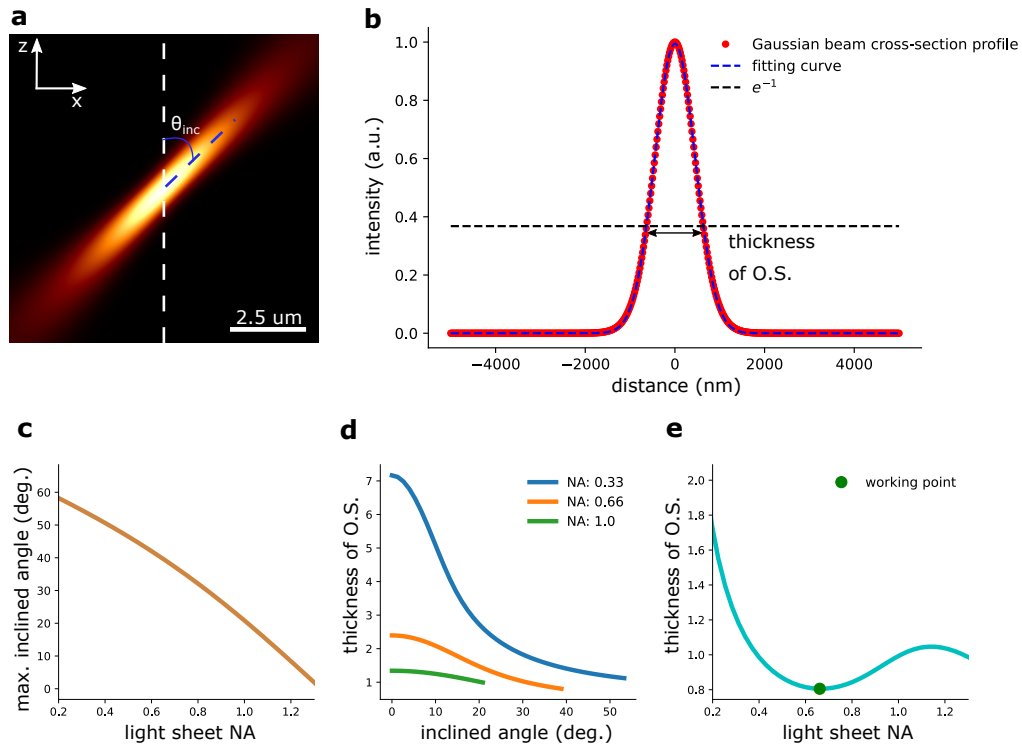


**Fig. 2.** Investigation of the system parameters versus the optical sectioning (O.S.) achieved by SOLEIL. (a) a simulated inclined Gaussian beam with 1 mm beam radius at the back focal plane and  $45^\circ$  inclined angle ( $\theta_{inc}$ ) from the optical axis of the objective lens (z-axis). We use the intensity profile along the white dashed line in (a) to determine the thickness of optical sectioning in (b). The O.S. thickness is determined at the position where the intensity drops down to  $e^{-1}$  (black dashed line). The red dots are the intensity values of the Gaussian beam along the white dash line in (a) and the blue dashed line is the fitting curve. (c) The SOLEIL light sheet NA versus the maximum inclined angle. (d) The optical sectioning versus the inclined angle (the angle between the beam and the optical axis). (e) The best optical sectioning for Gaussian beams with different NA. (c; green dot) The optimal optical sectioning is achieved at an NA of 0.66.

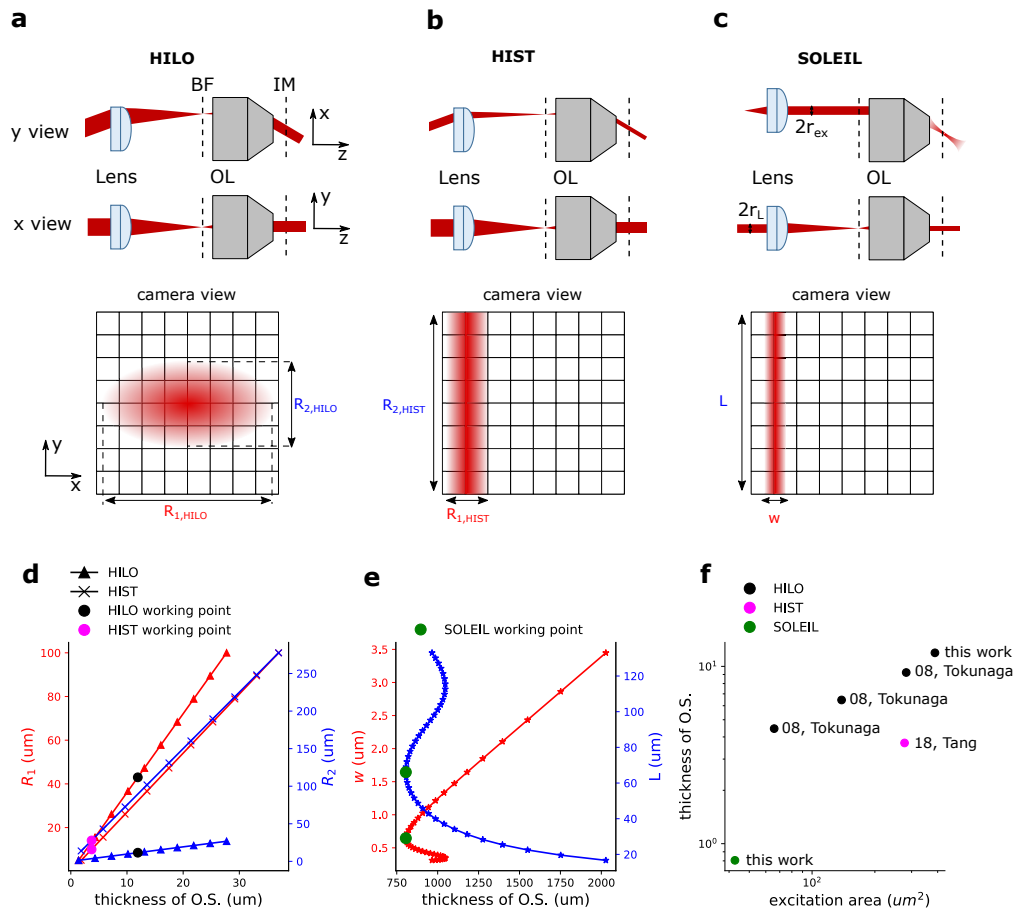


**Fig. 3.** Benchmark between HILO, HIST, and SOLEIL microscopy. (a)BF: back focal plane; IM: imaging plane; OL: objective lens. upper row: the schematic figure of HILO microscopy from x and y view. The z-axis stands for the optical axis of the objective lens. Lower row: camera view of HILO excitation profile at imaging plane.  $R_{1,HILO}$  the beamwidth of HILO at the imaging plane.  $R_{2,HILO}$  the original width of the HILO beam, which is not elongated by the inclination projection. (b) upper row: the schematic figure of HIST microscopy from x and y view. Lower row: camera view of HIST excitation profile at imaging plane. (c) upper row: the schematic figure of SOLEIL microscopy from x and y view. Lower row: camera view of the SOLEIL excitation profile at the imaging plane. L: length of SOLEIL light sheet,  $r_{ex}$ : the beam radius at the back focal plane of the objective lens, which determines the NA of Gaussian beam.  $r_L$ : the beam radius at the plane conjugated to the imaging plane, which can determine the length of SOLEIL profile (L). (d) the beam radius of HILO and HIST ( $R_1, R_2$ ) microscopy versus thickness of optical sectioning. (e) The beam dimension of SOLEIL versus the thickness of optical sectioning. The working point is the same as the working point in sub-figure Fig. 2 (c). (f) The benchmark of excitation area and thickness of optical sectioning between HILO, HIST, and SOLEIL. The data of HILO microscopy is from our HILO microscopy. The data of HIST microscopy is from the previous HIST paper [24]. The data of SOLEIL is from the working point in Fig. 2 (c).



kept at a fixed position during the exposure time before it is moved to the next position (Fig. 1 (h)). This increased exposure time will increase the acquired photons from the single-molecule until the molecule turns off, which improves the CRLB (supplementary section 6). The  $I/bg$  ratio decreases after a molecule has turned off, which deteriorates the estimated CRLB, which is shown in supplementary section 4. We observed that moving the light sheet slower than 20 ms will significantly decrease the  $I/bg$  ratio making it hard to process the data. In contrast to HIST microscopy, SOLEIL reads out whole camera frames (see section 2.8). To distinguish this difference, we termed the lateral displacement in HIST microscopy as sweeping and that of SOLEIL as stepping in Fig. 1 (c,d). The width of the SOLEIL light sheet ( $w$ ) is determined by the beam radius ( $r_{ex}$ ) at the back focal plane and the inclination angle from the optical axis of the objective lens Fig. 3 (c). The length of the SOLEIL light sheet ( $L$ ) is determined by the beam radius at the conjugated imaging plane before the objective  $L = 2r_L \cdot 3 \text{ mm}/200 \text{ mm}$ , where 200 mm is the focal length of lens in Fig. 3 (c) and 3 mm is the focal length of the objective lens. If no additional beam shaping is applied in the excitation path,  $r_L = r_{ex}$ .

In HILO, HIST, and SOLEIL microscopy, the size of the excitation area is coupled to the thickness of optical sectioning. In Fig. 3 (d), we show the trade-off curve between the beam radius ( $R_1, R_2$ ) and the thickness of optical sectioning of HILO and HIST microscopy. The inclined angle of HILO used for this simulation was chosen to be the same as the inclined angle of HILO setup used in our HILO system ( $74.5^\circ$ ). The HILO angle in the previously published paper was  $77^\circ$ , which was close to the angle in our setup. For HIST microscopy, we refer to the experiment parameters from the HIST paper [24]. The inclined angle of HIST is  $69.7^\circ$ , which is given by the inverse tangent of the ratio between the HIST beam width ( $R_{1,HIST} = 10 \mu\text{m}$ ) and the HIST beam thickness ( $dz=3.7 \mu\text{m}$ ). The relationship of beam width and beam thickness of HIST microscopy are the same as for HILO microscopy (see supplementary section 3). In the simulation, a constant inclined angle of HIST microscopy was chosen. In practice however, this angle changes over the FOV, which generates an in-homogeneous thickness of optical sectioning over the FOV [24].

In Fig. 3 (e), we show the trade-off curve of the SOLEIL between the width ( $w$ ), length ( $L$ ), and the thickness of optical sectioning (O.S.). With the data from Fig. 3 (d,e), we can evaluate the relationship between the excitation area and the thickness of the optical sectioning obtained by HILO, HIST and SOLEIL microscopy (Fig. 3 (f)). The HILO excitation area  $A_{HILO}$  was approximated as an ellipse and the area was calculated as  $A_{HILO} = \pi R_{1,HILO} \cdot R_{2,HILO}/4$ . The HIST excitation area  $A_{HIST}$  was calculated as  $A_{HIST} = R_{1,HIST} \cdot R_{2,HIST}$ . The SOLEIL excitation area  $A_{SOLEIL}$  was calculated as  $A_{SOLEIL} = L \cdot w$ .

The excitation area is a critical parameter that affects the total acquisition time of a SMLM acquisition. The total acquisition time is

$$T_{SMLM} = \frac{A_{de}}{A_{ex}} \cdot T_{exp} \cdot n_{iter}, \quad (1)$$

where  $A_{de}$  is the area of desired FOV,  $A_{ex}$  is the excitation area,  $T_{exp}$  is the exposure time per frame typically ranging from 10 ms ~ 50 ms, and  $n_{iter}$  is the number of iteration for the SMLM imaging typically larger than 1000 iteration. From the above formula, we know that a larger  $A_{ex}$  leads to faster SMLM imaging.

From the Fig. 3 (f), HILO microscopy delivers the largest excitation area compared to SOLEIL and HIST. SOLEIL microscopy offers the best optical sectioning at the cost of sacrificing the imaging speed. HIST microscopy has medium optical sectioning and a medium size of FOV. For the HILO and HIST microscopy, we want to note that the thickness of optical sectioning and excitation area vary depending on the inclined angle and input beam size. The data points in Fig. 3(f) come from our system and previous published research [20,24].

#### 2.4. Characterization of the SOLEIL excitation profile

To measure the excitation profile of our light sheet, we scanned a single fluorescence bead (23 nm; embedded in 1% agarose gel) in  $x$  and  $z$  with a stepsize of 270 nm. We estimated the light sheet profile by summing the signal acquired by the camera per scan position (see Fig.S2). The acquired signal from the bead was proportional to the excitation intensity and therefore gave an estimate of the light sheet profile. The light sheet profile was characterized by fitting the excitation intensities to an inclined Gaussian beam, by minimizing the mean squared error (MSE), resulting in a Gaussian beam waist ( $w_0$ ) and Rayleigh length ( $z_r$ ). The MSE was minimized using the Nelder-Mead algorithm [50]. The width and Rayleigh length of the Gaussian beam was estimated to be  $0.627 \mu\text{m}$  and  $1.929 \mu\text{m}$ , respectively (Fig.S3). The inclined angle was measured to be  $30^\circ$  from the optical axis of the objective lens in the environment with a refractive index of  $n = 1.33$ .

#### 2.5. Characterization of the HILO excitation profile

To characterize the HILO illumination, we acquired 200 frames images of fluorescent beads homogeneously embedded in 1% agarose gel (see section 2.10.1) at different FOVs. We used Super-resolution Microscopy Analysis Platform (SMAP, EMBL Heidelberg) [51] to localize the bead images to acquire the beads' position and intensity (Fig.S4). With this information, we built inertia matrix  $M$  and  $R_{1,\text{HILO}}$ ,  $R_{2,\text{HILO}}$  were obtained from the the eigenvalue of inertia matrix  $M$  (supplementary section 3). The HILO angle was the inverse cosine of the ratio between  $R_{1,\text{HILO}}$  and  $R_{2,\text{HILO}}$ . The beam thickness of HILO was estimated based on the  $R_{1,\text{HILO}}$  and the HILO angle.

#### 2.6. Computing the signal-to-background ratio (SBR) of agarose bead imaging

To benchmark the difference in optical sectioning performance, we imaged 23 nm fluorescent beads embedded in 1% agarose gel (see section 2.10.1) ( $>50 \mu\text{m}$ ) with widefield, HILO, and SOLEIL microscopy Fig. 1 (e-g). To obtain enough localizations to characterize the excitation profile we scanned the sample over the FOV. The SBR ratio was computed from the ratio between the estimated intensity and the estimated background of each bead. The estimation of intensity and background of beads was done by fitting the PSF with the Gaussian function, which is performed by using the SMAP platform.

The reported SBR (WF: 2.87; HILO: 10.85; SOLEIL: 18.50) in Fig. 1 (e-g) for widefield, HILO and SOLEIL were the median SBR obtained from 402 beads, 37078 beads, and 1054 beads, respectively. These were obtained by imaging multiple FOVs.

#### 2.7. Data acquisition

For all excitation modes, the sample was pre-bleached to reduce the density of molecules in the on-state. The pre-bleaching was done with widefield illumination for 30 to 60 seconds. For SOLEIL a simple data acquisition sequence was defined to acquire one full image at each light sheet step (i.e. we do not use a rolling shutter). The camera was used in external trigger mode and the camera and galvo mirror were synchronized by an Arduino micro-controller. All SOLEIL samples were imaged with a step size of  $0.375 \mu\text{m}$ , 36.3 - 44.43 frames per second, and with 20 - 25 ms exposure time per frame. These settings ensured that typically the full on-time of the molecule was captured before moving the light sheet. The impact of the exposure time on the signal to background ratio is shown in Fig.S5. The dSTORM data consists of 3000 ~ 10000 frames per step. Each sample was imaged with a specific number of steps, resulting in a different total stepped distance (2D/3D COS7:  $25 \mu\text{m}$ , HEK-293T:  $35 \mu\text{m}$ , Caco2-BBE:  $27 \mu\text{m}$ ) and size of the imaging FOV.

## 2.8. dSTORM data analysis

Super-resolution Microscopy Analysis Platform (SMAP, EMBL Heidelberg) was used for the 2D and 3D localization of single molecules [51]. In the 2D case, the width of the Gaussian PSF  $\sigma$  is taken as an additional parameter that needs to be estimated. The initial estimate of the width is set to  $\sigma = 1.6$  pixel, corresponding to 175 nm. We filtered out the localizations with an intensity lower than 200 photons and larger than 10000 photons and  $\sigma$  larger than 1.61 pixel. For the 3D localization, we calibrated a cubic-spline PSF model (supplementary section 7) with an experimentally obtained z-stack with 10 nm step size of fluorescence beads with 23 nm radius (Thermo Fisher Scientific, Tetraspeck). The drift correction was done by using the redundant cross-correlation method in SMAP [51,52].

## 2.9. Deformable mirror calibration using interferometric wavefront sensing

We used a Michelson interferometer to calibrate the deformable mirror (DM) [53]. The optical configuration of the interferometer is shown in Fig.S6 (a). The influence matrix was obtained by measuring the change in Zernike coefficients of the DM phase created with a push-pull cycle, with each actuator at 80% of the stroke range [54]. The interferometric DM calibration software from dmlib was used [55]. The phase information on the DM was captured within the interferogram fringes Fig.S6 (b). To extract the phase information from the interferogram fringe, the recorded interferogram fringe was transformed by fast Fourier transform (FFT), and three peaks were presented in the spatial frequencies domain Fig.S6 (c). Then, the software cropped the spatial frequencies around the first-order peak and shifted back to zero spatial frequency position. After that, the inverse FFT was used to transform the cropped spatial frequencies and the phase information was the angle of the complex number. With the phase information, we constructed the control matrix of DM.

To flatten the DM and to correct for system aberrations, we minimized the width of the PSF by minimizing the second moment of the PSF [56]:

$$M_{\text{sec}} = \sum_{i=0}^N \sum_{j=0}^N I(i,j) \cdot \left[ (i - c_x)^2 + (j - c_y)^2 \right], \quad (2)$$

where  $I(i,j)$  is the pixel value at row  $i$  and column  $j$  of a camera image of a single fluorescence bead,  $c_x$  and  $c_y$  are the center of mass of  $I(i,j)$ , and  $N$  is both the width and height of the camera image. We minimized the second moment of the PSF using the random walk algorithm [57] by imaging a single 23 nm fluorescence bead (Thermo Fisher Scientific, Tetraspeck). First, the control signal of the DM was perturbed by a random vector  $X$ , where each element  $X_k$  was drawn from a uniform distribution  $X_k \sim U(-0.025S_{\text{max}}, 0.025S_{\text{max}})$  with  $S_{\text{max}}$  as the maximum stroke of the DM. Subsequently, the second momentum of the PSF was measured, and if this input reduced the second moment, this new DM control signal was chosen as the new optimum. We repeated these steps until the algorithm converged to a stable point, typically after 500 iterations. This procedure was repeated two more times, and each time the stroke range was reduced by a factor of 2.

## 2.10. Sample preparation

### 2.10.1. Sample preparation fluorescence beads embedded in agarose gel

Agarose solution (1% w/v) was prepared in a glass bottle by adding 45 mg of Agarose powder (BP160-100, Thermo Fisher Scientific, Waltham MA, U.S.A.) to 4.5 mL of deionized (DI) water followed by 20 minutes stirring with a magnetic stirrer at 100 °C. Polystyrene 40 nm diameter microspheres labeled with a red fluorescent dye (633 nm excitation / 720 nm emission, Invitrogen TransFluoSphere T8870, Thermo Fisher Scientific) at 2% solid concentration was first lightly

ultra-sonicated to achieve a distributed dispersion of microspheres and aliquoted at 1:500 dilution with DI water. Then, 0.5 mL of this aliquot was added to the agarose solution and stirred for a further 10 minutes at 70 °C, giving a final concentration of 0.0004% solid microspheres by weight in agarose solution. Next, a standard microscope glass slide (25 mm x 75 mm x 1 mm, Thermo Fisher Scientific) and borosilicate glass coverslip (22 mm x 22 mm, #1.5 thickness, Merck KGaA, Darmstadt, Germany) were cleaned with ultra-sonication in acetone (5 minutes, Merck KGaA), DI water (5 minutes), isopropanol (5 minutes, Merck KGaA), DI water (5 minutes), and blow-dry with a compressed air gun. A few droplets of the agarose solution were placed on the glass slide using a plastic pipette, and the coverslip was immediately dropped on top. The specimen was left to cool for 10 minutes resulting in a solid agarose gel with embedded labeled microspheres. The coverslip was then sealed to the glass slide with nail polish.

#### 2.10.2. Caco2-BBE cells

Caco2-BBE cells (a gift from S.C.D. van IJzendoorn, University Medical Center Groningen, the Netherlands) were maintained in DMEM supplemented with 9% FBS (fetal bovine serum), 50 µg/µl penicillin/streptomycin and 2 mM L-glutamine at 37 °C and 5% CO<sub>2</sub>. Cells were seeded on 18 mm coverslips at a density of  $1 \cdot 10^5/\text{cm}^2$  and cultured for 10 to 12 days to allow for spontaneous polarization and brush border formation. Cells were fixed with 4% paraformaldehyde (PFA) in phosphate-buffered saline (PBS) for 10 minutes, washed with PBS (3 × 5 minutes), permeabilized with 0.5% Triton X-100 in Milli-Q water for 15 minutes, washed with PBS (3 × 5 minutes) and blocked with 3% BSA in PBS for at least 1 hour. Cells were incubated overnight at 4 °C with a primary antibody against ezrin (mouse, BD Biosciences, 610602, dilution 1:500). After washing in PBS (3 × 5 minutes), the cells were incubated with secondary antibody (goat, anti-Mouse IgG (H+L), Alexa Fluor 647 (Life Technologies, dilution 1:500) for 1 hour at room temperature (RT) and washed with PBS.

#### 2.10.3. COS-7 cells

COS-7 cells (a gift from Anna Akhmanova, Utrecht University, the Netherlands) were cultured at 37 °C and 5% CO<sub>2</sub> in DMEM, supplemented with 9% FBS and 1% penicillin/streptomycin. 24 hours after seeding them onto 18 mm #1.0 coverslips, cells were pre-extracted with 0.1% glutaraldehyde and 0.3% Triton-X100 in PEM80 (80 mM Pipes, 1mM EGTA, 4 mM MgCl<sub>2</sub>, pH 6.8) for 1 minute. The cells were subsequently fixed with 4% PFA and 4% sucrose in PEM80 for 10 minutes. After washing in PBS (3 × 5 minutes), cells were permeabilized in 0.25% Triton-X100 in PEM80 for 15 minutes. After washing (3 × 5 minutes), blocking was performed in 3% BSA in PEM80 for 1 hour, and cells were incubated overnight at 4 °C with a primary antibody against  $\alpha$ -tubulin (mouse IgG1, Sigma-Aldrich, B-5-1-2, dilution 1:1000 in blocking buffer). The cells were again washed with PBS (3 × 5 minutes) and incubated with a secondary antibody (goat, anti-Mouse IgG (H+L), Alexa Fluor 647 (Life Technologies, dilution 1:500 in blocking buffer) for 1 hour at RT and washed with PBS.

#### 2.10.4. HEK-293T cells

Human Embryonic Kidney cells (HEK-293T, DSMZ no. ACC 635) were cultured at 37 °C and 5% CO<sub>2</sub> in DMEM without phenol red supplemented with 4.5g/l glucose (Gibco, Thermo Fisher Scientific), 4 mM L-glutamine (Gibco, Thermo Fisher Scientific), 10% fetal bovine serum (Gibco, Thermo Fisher Scientific) and 1× penicillin-streptomycin (Gibco, Thermo Fisher Scientific). Cells were seeded on plasma treated 25 mm high-precision #1.5 borosilicate coverslips (Marienfeld) in 6-well plates (Thermo Fisher Scientific) 1 to 2 days before fixation.

The cells were washed twice in prewarmed DMEM without phenol red and then incubated for 90 seconds in prewarmed extraction buffer (MTSB2, 80 mM PIPES, 7 mM MgCl<sub>2</sub>, 1 mM EGTA, 150 mM NaCl, 5 mM D-glucose, KOH for tuning the pH to 6.8) with freshly added 0.3%

Triton X-100 and 0.25% glutaraldehyde. Subsequently, cells were fixed in prewarmed 4% PFA in MTSB2 for 10 minutes and washed with PBS ( $3 \times 5$  minutes). Then, cells were incubated with a freshly prepared solution PBS with 10 mM NaBH<sub>4</sub> for 7 minutes followed by washing in PBS ( $1 \times$  quick,  $2 \times 10$  minutes). Afterwards, cells were permeabilized in PBS with 0.25% Triton X-100 for 7 minutes and then blocked with blocking buffer (BB, 2% (w/v) BSA, 10 mM glycine, 50 mM NH<sub>4</sub>Cl in PBS pH 7.40 for 60 minutes at room temperature or overnight at 4°C. Blocked samples were incubated with anti-tubulin antibody (clone B-5-1-2 ascites fluid 1:200 dilution in BB, Sigma-Aldrich) at RT for 1 hour. Then, cells were washed with BB ( $3 \times 5$  minutes), followed by incubation with donkey anti-mouse Alexa Fluor 647 antibody (donkey anti-mouse (H+L) highly cross-adsorbed at 0.005 mg/ml in BB, Life Technologies) in the dark at RT for 1 hour. After washing with BB ( $3 \times 5$  minutes), samples were post-fixed by incubation with 2% PFA in  $1 \times$  PBS for 10 minutes, followed by washing with  $1 \times$  PBS ( $3 \times 5$  minutes).

#### 2.10.5. dSTORM buffer

For the dSTORM buffer, 84  $\mu$ l of 20 mM Tris (pH 8.0, Sigma-Aldrich) were freshly mixed with 10  $\mu$ l of 1M MEA (Sigma-Aldrich), 5  $\mu$ l of 50% w/v Glucose stock, and 1  $\mu$ l of Glucose Oxygen Scavenging buffer (70 mg/ml glucose oxidase (Sigma-Aldrich) and 4 mg/ml catalase (Sigma-Aldrich) in Milli-Q water [58]). The coverslip with cells was mounted on a cavity microscope slide with a 25 mm dent (Sigma-Aldrich, BR475505). 75  $\mu$ l dSTORM buffer was deposited in the microscope slide dent. The surplus of dSTORM buffer was removed using lens tissue. Next, we carefully sealed the coverslip with silicone-gel Twinsil (Picodent, Wipperfurth). When applying the silicone gel around the coverslip, no liquid should be present around the coverslip, otherwise, it is more difficult to harden the silicone gel. After 20 minutes, the silicone gel was dry and the sample was ready for measuring.

### 3. Results

#### 3.1. COS-7 tubulin dSTORM imaging

We benchmarked SOLEIL against widefield excitation by imaging COS-7 cells labeled with Alexa Fluor 647. The light sheet had an incline angle of 30° and the exposure time was 25 ms. In the SOLEIL experiment, the laser intensity was adjusted to make the single-molecule intensity match the intensity obtained from widefield mode. The total stepped distance and FOV of SOLEIL were 25  $\mu$ m and 25  $\mu$ m  $\times$  45  $\mu$ m, respectively. For the benchmark, we did not use a CRLB filter to warrant an unbiased estimate of the intensity to background ratio ( $I/bg$ ). Using the SOLEIL improved the median value of the  $I/bg$  ratio from 10.03 to 84.22 compared with widefield illumination (Fig. 4 (g)). In widefield microscopy, the median value of localization intensity was 585 photons and in SOLEIL the median value of localization intensity was 468 photons (Fig. 4 (i)). The median background of widefield microscopy was 58.30 photons/pixel and the median background of SOLEIL was 5.71 photons/pixel (Fig. 4 (h)). We performed a simulation to demonstrate that optimization of the  $I/bg$  ratio can improve the CRLB by 72.5% when the intensities are the same (Fig.S7 (a,b)). In Fig. 4 (d), the estimated CRLB improvement was 57% because the localizations of the SOLEIL data had lower photon counts on average than for the widefield data. For the widefield data, the median value of localization intensity was 585 photons, whereas for SOLEIL data it was 468 photons (Fig. 4 (i)). The total number of localizations acquired was  $\approx 1.3 \cdot 10^6$  and  $\approx 7.5 \cdot 10^5$  for widefield and SOLEIL microscopy, resp., which corresponds to  $\approx 3.0 \cdot 10^5$  localizations/min in widefield microscopy and  $\approx 9.5 \cdot 10^3$  localizations/min in SOLEIL microscopy.

To enable 3D SMLM, we used the deformable mirror to introduce an astigmatic aberration, of which the resulting PSF and CRLB curve are shown in Fig.S8. In this case, the background fluorescence for SOLEIL was lower than the background for widefield illumination, which results



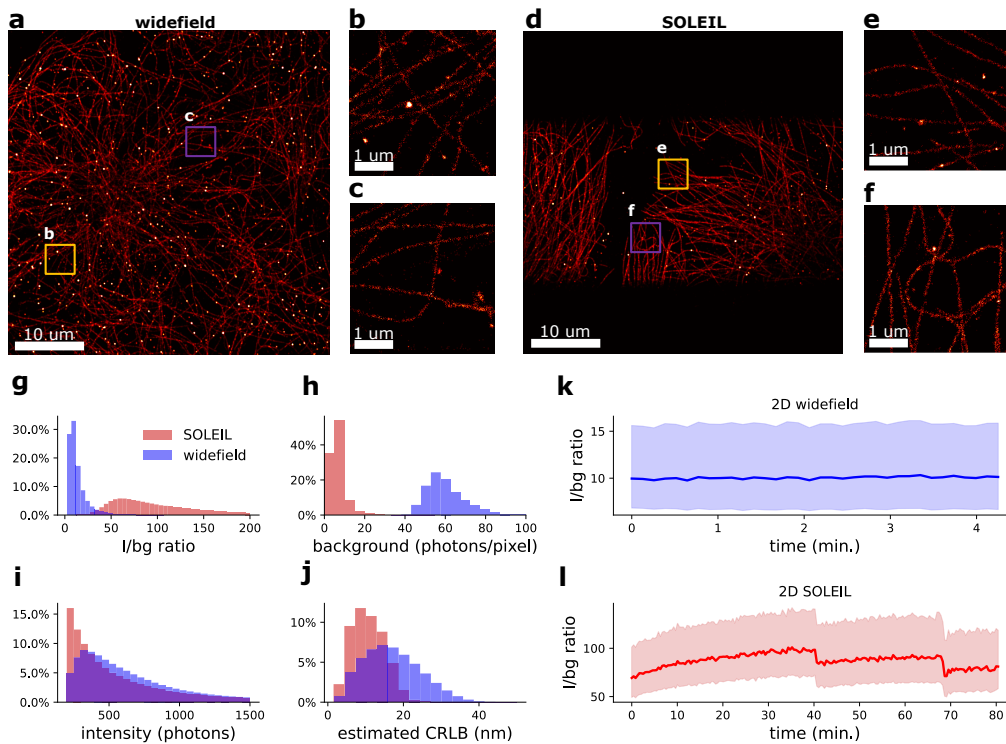


**Fig. 4.** 2D super-resolution image of a COS-7 tubulin. The imaging depth was  $<1 \mu\text{m}$  for (a,d). (a) 2D super-resolution image with the microscope in widefield mode. (b,c) Zoom-in of (a). (d) 2D localization image with the microscope in SOLEIL mode, with  $25 \mu\text{m}$  total stepped distance. (e,f) Zoom in image of (d). (g-j) Benchmark of intensity to background ratio, background, intensity, and estimated CRLB between widefield and SOLEIL. (k,l) I/bg ratios of widefield mode and SOLEIL mode over experiment time. The opaque colored region represents the first quartile to the third quartile.

in an improved estimated CRLB. Based on the measured localizations, we found that the median I/bg ratio was improved from 22 to 230 (Fig. 5 (g)). Using SOLEIL the average lateral and axial CRLB improved 200% compared with widefield illumination (Fig. 5 (j,k)). The median value of localization intensity was 1416 photons and 737 photons, for widefield and SOLEIL illumination, resp. (Fig. 5 (i)), whereas the median background was 65 photons/pixel and 2.59 photons/pixel (Fig. 5 (h)). The footprint of an astigmatic PSF is larger than that of a Gaussian PSF, and therefore spots needed a higher intensity to pass the spot detection threshold. For this reason, we performed a longer experiment to accumulate enough high-intensity spots, as the low-intensity spots were not detected by the spot detection algorithm. The total number of localizations acquired was  $\approx 3.9 \cdot 10^5$  and  $\approx 3.7 \cdot 10^5$  for widefield and SOLEIL illumination, resp. This corresponds to  $\approx 3.1 \cdot 10^4$  localizations/min in widefield microscopy and  $\approx 2.1 \cdot 10^3$  localizations/min in SOLEIL microscopy.

### 3.2. HEK-293T tubulin and Caco-2-BBE ezrin dSTORM imaging

We chose HEK-293T and Caco-2-BBE cells to demonstrate the capacity to image thick samples. The thickness of cells are  $\approx 9 \mu\text{m}$  and  $\approx 15 \mu\text{m}$  [59], respectively. For HEK-293T and Caco2-BBE cells, we used SOLEIL microscopy that had an incline angle of  $30^\circ$  from the optical axis of the objective lens. The angle of HILO we used in HEK-293T and Caco2-BBE sample imaging

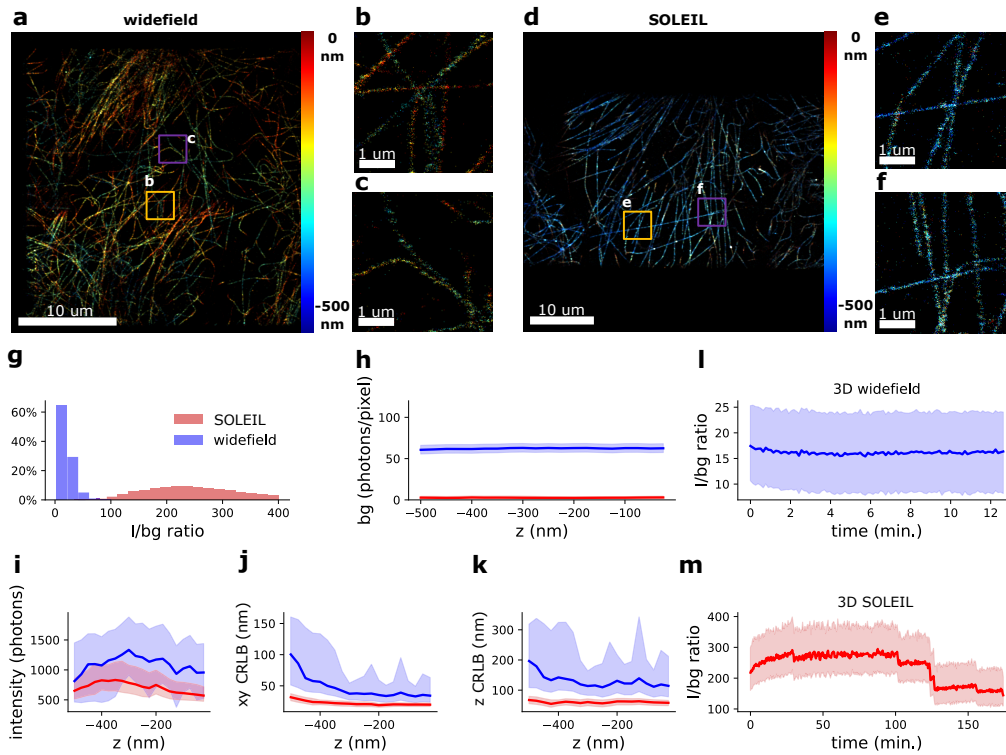


**Fig. 5.** 3D super-resolution image of COS-7 tubulin. The imaging depth was  $<1 \mu\text{m}$  for (a,d). (a) 3D super-resolution image with the microscope in widefield mode. (b,c) Zoom-in of (a). (d) 3D super-resolution image with with the microscope in SOLEIL mode, with  $25 \mu\text{m}$  total stepped distance. (e,f) Zoom-in of (d). (g-k) Benchmark of I/bg ratio, background, intensity, and estimated CRLB between widefield mode and SOLEIL mode. The opaque color region represents the first quartile to the third quartile. (l,m) I/bg ratios of widefield mode and SOLEIL mode over experiment time. The opaque color region represents the first quartile to the third quartile.

was  $74.5^\circ$  and the HILO beam width ( $R_{1,\text{HILO}}$ ) was  $43 \mu\text{m}$ . In the HEK-293T sample, the exposure time of widefield, HILO, and SOLEIL were both 25 ms. In Caco2-BBE cells imaging, the angle for SOLEIL microscopy was the same as the SOLEIL angle we used for HEK-293T cells imaging. The exposure times were 20 ms, 25 ms, and 25 ms for widefield, HILO and SOLEIL illumination resp. The total stepped distance and FOV were  $35 \mu\text{m}$  and  $35 \mu\text{m} \times 35 \mu\text{m}$ , respectively. For the HEK-293T sample, the median I/bg ratio acquired by widefield microscopy was 7.50, the median I/bg ratio acquired by HILO microscopy was 13.06, and the median I/bg ratio acquired by SOLEIL microscopy was 31.39 (Fig. 6 (j)). The median estimated CRLB acquired by widefield microscopy was 18.88 nm, the median estimated CRLB acquired by HILO microscopy was 15.90 nm, and the median estimated CRLB acquired by SOLEIL microscopy was 12.20 nm (Fig. 6 (m)). We observed a 400% higher I/bg ratio and 54% improvement of estimated CRLB in the benchmark between SOLEIL and widefield microscopy and a 240% higher I/bg ratio and 30% improvement of estimated CRLB in the benchmark between SOLEIL and HILO microscopy (Fig. 6 (j,m)). In the widefield microscopy, the median value of localization intensity was 507 photons, in HILO was 608 photons and in SOLEIL was 508 photons (Fig. 6 (l)). The median background of widefield microscopy was 69 photons/pixel, the median background of HILO was 48 photons/pixel and the median background of SOLEIL was 17 photons/pixel (Fig. 6

(k)). The total number of localization acquired by widefield microscopy was  $\approx 3.1 \cdot 10^5$ , the total number of localization acquired by HILO microscopy was  $\approx 1.6 \cdot 10^5$  and the total number of localization acquired by SOLEIL microscopy was  $\approx 6.4 \cdot 10^5$ , which corresponds to  $\approx 1.8 \cdot 10^5$  localizations/min in widefield microscopy,  $\approx 3.0 \cdot 10^4$  localizations/min in HILO microscopy and  $\approx 9.4 \cdot 10^3$  localizations/min in SOLEIL microscopy.

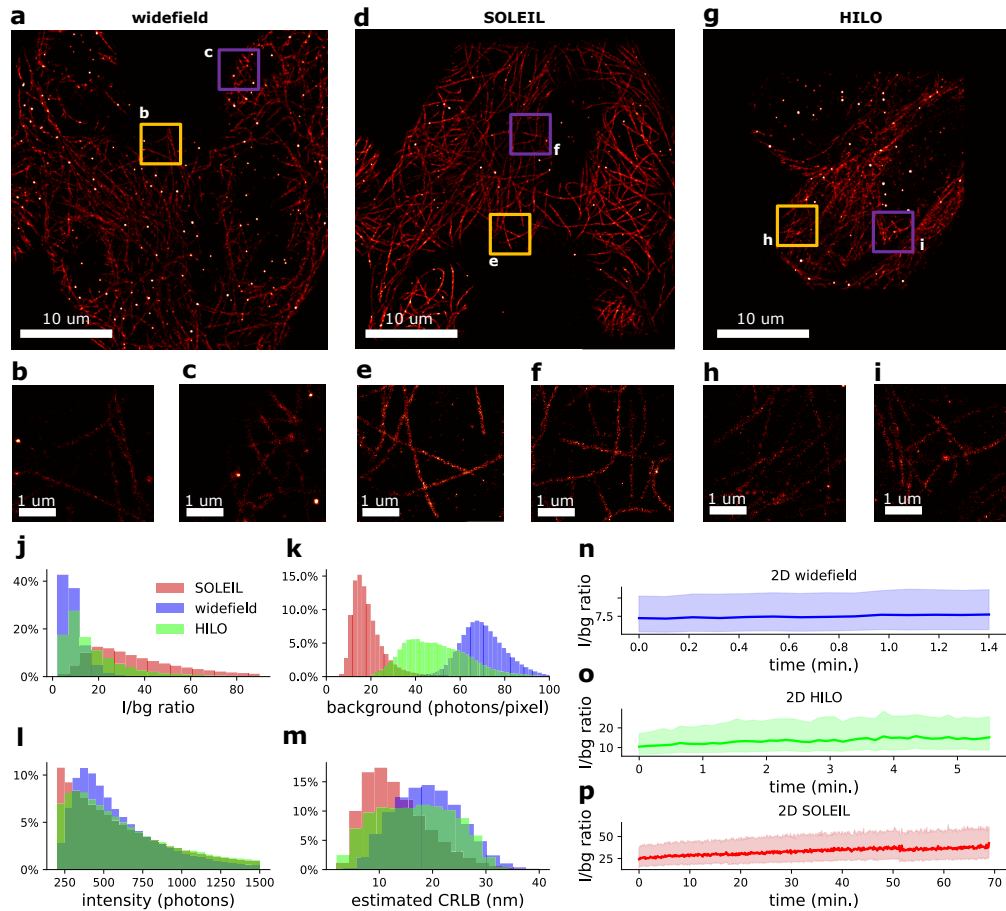


**Fig. 6.** 2D super-resolution image of HEK-293T tubulin. The imaging depth was approximately  $5 \mu\text{m}$  for (a,d,g). (a) 2D super-resolution reconstruction from widefield imaging data. (b,c) Zoom-in of (a). (d) 2D localization reconstruction from SOLEIL imaging data, with a  $35 \mu\text{m}$  total stepped distance. (e,f) Zoom-in image of (d). (g) 2D localization reconstruction from HILO imaging data. (h,i) Zoom-in image of (g). (j-m) Benchmark of I/bg ratio, background, intensity, and estimated CRLB between widefield, HILO, and SOLEIL microscopy. (n-p) I/bg ratios for widefield, HILO, and SOLEIL microscopy over experiment time. The opaque color region represents the first quartile to the third quartile.

For the Caco-2-BBE sample, the median I/bg ratio acquired by widefield microscopy was 13.06, the median I/bg ratio acquired by HILO microscopy was 26.48, and the median I/bg ratio acquired by SOLEIL microscopy was 48.86 (Fig. 7 (j)). The median estimated CRLB acquired by widefield microscopy was 21.93 nm, the median estimated CRLB acquired by HILO microscopy was 17.12 nm, and the median estimated CRLB acquired by SOLEIL microscopy was 14.26 nm (Fig. 7 (m)). We observed a 374% higher I/bg ratio and 54% improvement of estimated CRLB in the benchmark between SOLEIL and widefield microscopy and a 184% higher I/bg

ratio and 20% improvement of estimated CRLB in the benchmark between SOLEIL and HILO microscopy (Fig. 7 (j,m)). The median value of the estimated intensity was with widefield microscopy 303 photons, with HILO microscopy 325 photons, and with SOLEIL 345 photons (Fig. 7 (l)). The median value of the estimated background was with widefield microscopy 23 photons/pixel, with HILO microscopy 12.7 photons/pixel, and with SOLEIL 7 photons/pixel (Fig. 7 (k)). The total number of localization acquired with widefield microscopy was  $\approx 1.1 \cdot 10^5$ , with HILO microscopy  $\approx 1.0 \cdot 10^5$ , and with SOLEIL microscopy  $\approx 1.4 \cdot 10^5$ . This corresponds to  $\approx 3.2 \cdot 10^4$  localizations/min with widefield microscopy,  $\approx 3.0 \cdot 10^4$  localizations/min with HILO microscopy and  $\approx 5.6 \cdot 10^3$  localizations/min with SOLEIL microscopy.

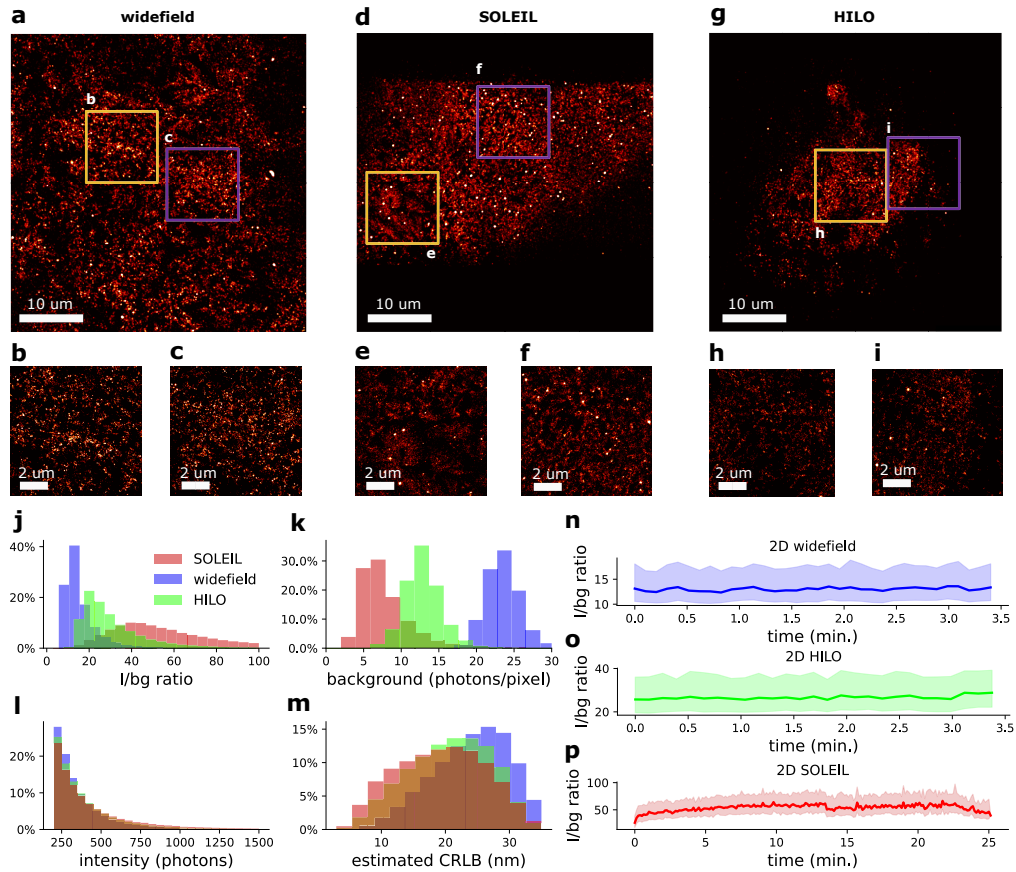


**Fig. 7.** 2D super-resolution reconstruction of Caco2-BBE ezrin. The imaging depth was approximately 8 - 10  $\mu\text{m}$  for (a,d,g) (a) 2D super-resolution reconstruction from widefield imaging data. (b,c) Zoom-in of (a). (d) 2D super-resolution reconstruction from SOLEIL imaging data, with a 27  $\mu\text{m}$  total stepped distance. (e,f) Zoom-in image of (d). (g) 2D super-resolution reconstruction from HILO imaging data. (h,i) Zoom-in image of (g). (j-m) Benchmark of I/bg ratio, background, intensity, and estimated CRLB for widefield, HILO, and SOLEIL microscopy. (n-p) I/bg ratios of for widefield, HILO, and SOLEIL microscopy over experiment time. The opaque colored region represents the first quartile to the third quartile.

#### 4. Discussion and conclusion

To achieve a better SMLM resolution in thick samples, it is essential to minimize background fluorescence. Minimizing background fluorescence can improve the CRLB in SMLM (Fig.S7 (a)). TIRF microscopy shows excellent background rejection capabilities, but the short illumination depth limits its applicability to thin samples. HILO and HIST microscopy achieve optical sectioning using only a single objective. However, the performance of the optical sectioning of these methods are typically worse than light sheet microscopy. SPIM and soSPIM approaches have a limited detection and/or illumination NA and require custom-made sample holders. To avoid these drawbacks, we developed a novel single objective lens inclined light sheet platform, SOLEIL. SOLEIL has no constraints for sample mounting and avoids the restriction on the NA. We demonstrated this on HEK-293T and Caco-2-BBE cells with a thickness of  $\approx 9 \mu\text{m}$  and  $\approx 15 \mu\text{m}$ , respectively.

Our simulations showed that the optimal optical sectioning of SOLEIL is at 0.66 excitation NA and can reach  $0.8 \mu\text{m}$  optical sectioning, which is around four times larger than the thickness of optical sectioning of TIRF microscopy ( $\approx 200 \text{ nm}$ ). We experimentally measured the excitation profile of our microscope. The measured width of an inclined Gaussian beam is  $0.627 \mu\text{m}$  while the theoretical width is  $0.346 \mu\text{m}$ . We hypothesize that the difference between the measured and theoretical spot sizes is caused by multiple laser modes and aberrations in the system, which enlarges the inclined Gaussian beam width. The laser can be cleaned using a pinhole or a single-mode fiber, and aberrations can be minimized by selecting optimal lenses using sophisticated optical software such as Zemax. This could lead to a performance that is closer to the theoretical value, but this has not been investigated in the current study since most of the information about the objective lens is proprietary information.

We have demonstrated that SOLEIL performs effective optical sectioning in thick samples with a FOV that is comparable to soSPIM; as previously reported:  $19 \mu\text{m} \times 37 \mu\text{m}$  [32],  $10.8 \mu\text{m} \times 25.7 \mu\text{m}$  [33], and  $10 \mu\text{m} \times 19 \mu\text{m}$  [34]. To demonstrate this, we have imaged COS-7 samples in 2D and 3D with an FOV of  $25 \mu\text{m} \times 45 \mu\text{m}$ .

We experimentally investigated the difference of optical sectioning between SOLEIL, widefield, and HILO microscopy. The experimental benchmark was done with 23 nm fluorescent beads embedded in 1% agarose gel. We showed that the SBR ratio of SOLEIL improved 80% over HILO microscopy and improved 540% over widefield microscopy. The benefits of SOLEIL over the other illumination schemes (widefield and HILO) have also been demonstrated with several dSTORM samples. With the dSTORM experiments, we showed that the I/bg ratio and the estimated CRLB were significantly improved when using SOLEIL instead of widefield and HILO illumination. We found that the use of SOLEIL significantly improved the distribution of the I/bg ratio and SOLEIL does not suffer in the same way from the trade-off between FOV and optical sectioning like HILO, SPIM, and soSPIM. The I/bg ratio of SOLEIL was 3.5 to 8.5 times better than that of the widefield illumination (Fig. 4,5 (g), Fig. 6,7 (j)). This observation was reproducible in all SOLEIL SMLM imaging (Fig.S9,10). We observed that the labeling density and labeled protein of dSTORM sample can affect background fluorescence. We observed that this effect can be more significant than increasing the sample thickness. For example, we obtained a median I/bg ratio of 10.03 in the 2D COS-7 sample with widefield microscopy and a median I/bg ratio of 13.06 in the 2D Caco2-BBE sample with widefield microscopy. In some SOLEIL experiments, we observed that the I/bg ratio was not a smooth curve, but that the I/bg ratio drops at some arbitrary moments in time (Fig. 4 (l), 5 (m)). One potential explanation for this is the stability of the stage (supplementary section 9). When the imaging plane is close to the coverslip and the sample drifts away from the objective lens, the sample is excited by a part of the light sheet further away from the center, where the beam width is larger. This changes the excitation condition and can change I/bg ratio. We experimentally validated our assumption by purposely



drifting the sample away from the objective lens, and indeed we observed a drop in the  $I/bg$  ratio curve (Fig.S11). We believe this can be mitigated by implementing z-stabilization.

In Fig.S5, we performed dSTORM imaging by using SOLEIL microscopy with different exposure times to investigate how exposure time affects the  $I/bg$  ratio and the estimated CRLB. We observed that long exposure time deteriorates the  $I/bg$  ratio, which can result in a worse CRLB. A possible reason is that the exposure time is longer than the average on-time of the molecule and therefore only background photons are acquired once the molecule has turned off.

Fig. 3 (d,f) shows the trade-off between the size of FOV and the optical sectioning of HILO microscopy, similar to previous work [20]. We benchmarked the performance of optical sectioning for HILO with a small and large FOV by use of dSTORM imaging with Caco2-BBE cell (Fig.S12). We observed that the  $I/bg$  ratio of large FOV HILO was lower than that of small FOV HILO (Fig.S12 (c)). This illustrates the trade-off relationship between FOV and optical sectioning of HILO in dSTORM sample.

SOLEIL can be extended with more advanced features to increase the acquisition speed and FOV. For example, scanning with multiple parallel light sheets will massively increase the acquisition speed and FOV. These parallel light sheets can be created by diffraction of optical elements [60]. Furthermore, we envision that the DM can be used for adaptive optics (AO) to correct system aberrations when imaging thick samples and that the average fluorescence intensity and blinking rate can be optimized through real-time adaptive control of the light sheet intensity. We believe that SOLEIL will become an important approach for SMLM samples where optical sectioning and aberration correction is essential.

**Funding.** Netherlands Organisation for Scientific Research (NWO), under NWO START-UP project no. 740.018.015, NOW Veni project no. 16761, FOM Neurophotonics project no. 16NEPH01.

**Acknowledgments.** The authors would like to thank Y. Deurloo and C. Pereira Frias for assisting us with the cell culture. The authors would like to thank D. Brinks for using his lab for sample preparation.

S.H., J.C. D.F., and C.S.S. were supported by the Netherlands Organisation for Scientific Research (NWO), under NWO START-UP project no. 740.018.015 and NWO Veni project no. 16761. M.S., D.J., and L.C.K. were supported by NWO, under FOM Neurophotonics project no. 16NEPH01.

**Disclosures.** The authors declare no conflicts of interest.

**Data availability.** The original image data is available upon reasonable request.

**Supplemental document.** See [Supplement 1](#) for supporting content.

## References

1. S. T. Hess, T. P. Girirajan, and M. D. Mason, "Ultra-high resolution imaging by fluorescence photoactivation localization microscopy," *Biophys. J.* **91**(11), 4258–4272 (2006).
2. G. Manley S. Gillette J. Patterson, "High-density mapping of single-molecule trajectories with photoactivated localization microscopy," *Nat. Methods* **5**(2), 155–157 (2008).
3. E. Betzig, G. H. Patterson, R. Sougrat, O. W. Lindwasser, S. Olenych, J. S. Bonifacino, M. W. Davidson, J. Lippincott-Schwartz, and H. F. Hess, "Imaging intracellular fluorescent proteins at nanometer resolution," *Science* **313**(5793), 1642–1645 (2006).
4. A. Egner, C. Geisler, C. Von Middendorff, H. Bock, D. Wenzel, R. Medda, M. Andresen, A. Stiel, S. Jakobs, C. Eggeling, A. Schönle, and S. Hell, "Fluorescence nanoscopy in whole cells by asynchronous localization of photoswitching emitters," *Biophys. J.* **93**(9), 3285–3290 (2007).
5. K. A. Lidke, B. Rieger, T. M. Jovin, and R. Heintzmann, "Superresolution by localization of quantum dots using blinking statistics," *Opt. Express* **13**(18), 7052–7062 (2005).
6. C. Smith, B. Joseph, and N. Rieger, "Fast, single-molecule localization that achieves theoretically minimum uncertainty," *Nat. Methods* **7**(5), 373–375 (2010).
7. R. P. J. Nieuwenhuizen, K. A. Lidke, M. Bates, D. L. Puig, D. Grünwald, S. Stallinga, and B. Rieger, "Measuring image resolution in optical nanoscopy," *Nat. Methods* **10**(6), 557–562 (2013).
8. R. J. Ober, S. Ram, and E. S. Ward, "Localization accuracy in single-molecule microscopy," *Biophys. J.* **86**(2), 1185–1200 (2004).
9. C. S. Smith, S. Stallinga, K. A. Lidke, B. Rieger, and D. Grünwald, "Probability-based particle detection that enables threshold-free and robust in vivo single-molecule tracking," *Mol. Biol. Cell* **26**(22), 4057–4062 (2015).
10. C. S. Smith, K. Jouravleva, M. Huisman, S. M. Jolly, P. D. Zamore, and D. Grünwald, "An automated bayesian pipeline for rapid analysis of single-molecule binding data," *Nat. Commun.* **10**(1), 272 (2019).

11. T. Cowen, A. J. Haven, and G. Burnstock, "Pontamine sky blue: A counterstain for background autofluorescence in fluorescence and immunofluorescence histochemistry," *Histochemistry* **82**(3), 205–208 (1985).
12. J. Bierwagen, I. Testa, J. Fölling, D. Wenzel, S. Jakobs, C. Eggeling, and S. W. Hell, "Far-field autofluorescence nanoscopy," *Nano Lett.* **10**(10), 4249–4252 (2010).
13. B. Clancy and L. Cauller, "Reduction of background autofluorescence in brain sections following immersion in sodium borohydride," *J. Neurosci. Methods* **83**(2), 97–102 (1998).
14. J. R. Mansfield, K. W. Gossage, C. C. Hoyt, and R. M. Levenson, "Autofluorescence removal, multiplexing, and automated analysis methods for in-vivo fluorescence imaging," *J. Biomed. Opt.* **10**(4), 041207 (2005).
15. J. M. Murray, P. L. Appleton, J. R. Swedlow, and J. C. Waters, "Evaluating performance in three-dimensional fluorescence microscopy," *J. Microsc.* **228**(3), 390–405 (2007).
16. J. Mertz and J. Kim, "Scanning light-sheet microscopy in the whole mouse brain with HiLo background rejection," *J. Biomed. Opt.* **15**(1), 016027 (2010).
17. J. G. White, W. B. Amos, and M. Fordham, "An evaluation of confocal versus conventional imaging of biological structures by fluorescence light microscopy," *J. Cell Biol.* **105**(1), 41–48 (1987).
18. D. Axelrod, "Total internal reflection fluorescence microscopy in cell biology," *Traffic* **2**(11), 764–774 (2001).
19. H. Schneckenburger, "Total internal reflection fluorescence microscopy: technical innovations and novel applications," *Curr. Opin. Biotechnol.* **16**(1), 13–18 (2005).
20. M. Tokunaga, N. Imamoto, and K. Sakata-Sogawa, "Highly inclined thin illumination enables clear single-molecule imaging in cells," *Nat. Methods* **5**(2), 159–161 (2008).
21. C. A. Konopka and S. Y. Bednarek, "Variable-angle epifluorescence microscopy: a new way to look at protein dynamics in the plant cell cortex," *The Plant J.* **53**(1), 186–196 (2008).
22. R. Jungmann, M. S. Avendaño, J. B. Woehrstein, M. Dai, W. M. Shih, and P. Yin, "Multiplexed 3D cellular super-resolution imaging with dna-paint and exchange-paint," *Nat. Methods* **11**(3), 313–318 (2014).
23. S. Liu, H. Huh, S.-H. Lee, and F. Huang, "Three-dimensional single-molecule localization microscopy in whole-cell and tissue specimens," *Annu. Rev. Biomed. Eng.* **22**(1), 155–184 (2020).
24. J. Tang and K. Y. Han, "Extended field-of-view single-molecule imaging by highly inclined swept illumination," *Optica* **5**(9), 1063–1069 (2018).
25. M. B. Ahrens, M. B. Orger, D. N. Robson, J. M. Li, and P. J. Keller, "Whole-brain functional imaging at cellular resolution using light-sheet microscopy," *Nat. Methods* **10**(5), 413–420 (2013).
26. C.-H. Lu, W.-C. Tang, Y.-T. Liu, S.-W. Chang, F. C. M. Wu, C.-Y. Chen, Y.-C. Tsai, S.-M. Yang, C.-W. Kuo, Y. Okada, Y.-K. Hwu, P. Chen, and B.-C. Chen, "Lightsheet localization microscopy enables fast, large-scale, and three-dimensional super-resolution imaging," *Commun. Biol.* **2**(1), 177 (2019).
27. K. M. Dean, P. Roudot, E. S. Welf, G. Danuser, and R. Fiolka, "Deconvolution-free subcellular imaging with axially swept light sheet microscopy," *Biophys. J.* **108**(12), 2807–2815 (2015).
28. A.-K. Gustavsson, P. N. Petrov, and W. E. Moerner, "Light sheet approaches for improved precision in 3D localization-based super-resolution imaging in mammalian cells," *Opt. Express* **26**(10), 13122–13147 (2018).
29. A.-K. Gustavsson, P. N. Petrov, M. Y. Lee, Y. Shechtman, and W. E. Moerner, "3d single-molecule super-resolution microscopy with a tilted light sheet," *Nat. Commun.* **9**(1), 123 (2018).
30. T. C. Fadero, T. M. Gerbich, K. Rana, A. Suzuki, M. DiSalvo, K. N. Schaefer, J. K. Heppert, T. C. Boothby, B. Goldstein, M. Peifer, N. L. Allbritton, A. S. Gladfelter, A. S. Maddox, and P. S. Maddox, "LITE microscopy: Tilted light-sheet excitation of model organisms offers high resolution and low photobleaching," *J. Cell Biol.* **217**(5), 1869–1882 (2018).
31. B. Migliori, M. S. Datta, C. Dupre, M. C. Apak, S. Asano, R. Gao, E. S. Boyden, O. Hermanson, R. Yuste, and R. Tomer, "Light sheet theta microscopy for rapid high-resolution imaging of large biological samples," *BMC Biol.* **16**(1), 57 (2018).
32. M. B. M. Meddens, S. Liu, P. S. Finnegan, T. L. Edwards, C. D. James, and K. A. Lidke, "Single objective light-sheet microscopy for high-speed whole-cell 3D super-resolution," *Biomed. Opt. Express* **7**(6), 2219–2236 (2016).
33. R. Galland, G. Greci, A. Aravind, V. Viasnoff, V. Studer, and J.-B. Sibarita, "3D high- and super-resolution imaging using single-objective spim," *Nat. Methods* **12**(7), 641–644 (2015).
34. E. Zagato, T. Brans, S. Verstuyft, D. van Thourhout, J. Missinne, G. van Steenberge, J. Demeester, S. D. Smedt, K. Remaut, K. Neyts, and K. Braeckmans, "Microfabricated devices for single objective single plane illumination microscopy (sospim)," *Opt. Express* **25**(3), 1732–1745 (2017).
35. M. Kumar and Y. Kozorovitskiy, "Tilt-invariant scanned oblique plane illumination microscopy for large-scale volumetric imaging," *Opt. Lett.* **44**(7), 1706–1709 (2019).
36. M. Kumar and Y. Kozorovitskiy, "Tilt (in)variant lateral scan in oblique plane microscopy: a geometrical optics approach," *Biomed. Opt. Express* **11**(6), 3346–3359 (2020).
37. V. Voleti, K. B. Patel, W. Li, C. Perez Campos, S. Bharadwaj, H. Yu, C. Ford, M. J. Casper, R. W. Yan, W. Liang, C. Wen, K. D. Kimura, K. L. Targoff, and E. M. C. Hillman, "Real-time volumetric microscopy of in vivo dynamics and large-scale samples with scape 2.0," *Nat. Methods* **16**(10), 1054–1062 (2019).
38. S. An, K. F. Ziegler, P. Zhang, Y. Wang, T. Kwok, F. Xu, C. Bi, S. Matosevic, P. Yin, T. Li, and F. Huang, "Axial plane single-molecule super-resolution microscopy of whole cells," *Biomed. Opt. Express* **11**(1), 461–479 (2020).

39. B. Yang, X. Chen, Y. Wang, S. Feng, V. Pessino, N. Stuurman, N. H. Cho, K. W. Cheng, S. J. Lord, L. Xu, D. Xie, R. D. Mullins, M. D. Leonetti, and B. Huang, "Epi-illumination spim for volumetric imaging with high spatial-temporal resolution," *Nat. Methods* **16**(6), 501–504 (2019).
40. C. Dunsby, "Optically sectioned imaging by oblique plane microscopy," *Opt. Express* **16**(25), 20306 (2008).
41. J. Tang and K. Y. Han, "Low-photobleaching line-scanning confocal microscopy using dual inclined beams," *J. Biophotonics* **12**(10), e201900075 (2019).
42. M. B. Sikkell, S. Kumar, V. Maioli, C. Rowlands, F. Gordon, S. E. Harding, A. R. Lyon, K. T. MacLeod, and C. Dunsby, "High speed scmos-based oblique plane microscopy applied to the study of calcium dynamics in cardiac myocytes," *J. Biophotonics* **9**(3), 311–323 (2016).
43. H. Sparks, L. Dent, C. Bakal, A. Behrens, G. Salbreux, and C. Dunsby, "Dual-view oblique plane microscopy (dopm)," *Biomed. Opt. Express* **11**(12), 7204–7220 (2020).
44. M. B. Bouchard, V. Voleti, C. S. Mendes, C. Lacefield, W. B. Grueber, R. S. Mann, R. M. Bruno, and E. M. C. Hillman, "Swept confocally-aligned planar excitation (scape) microscopy for high-speed volumetric imaging of behaving organisms," *Nat. Photonics* **9**(2), 113–119 (2015).
45. M. Kumar, S. Kishore, J. Nasenbeny, D. L. McLean, and Y. Kozorovitskiy, "Integrated one- and two-photon scanned oblique plane illumination (sopi) microscopy for rapid volumetric imaging," *Opt. Express* **26**(10), 13027–13041 (2018).
46. S. Kumar, D. Wilding, M. B. Sikkell, A. R. Lyon, K. T. MacLeod, and C. Dunsby, "High-speed 2D and 3D fluorescence microscopy of cardiac myocytes," *Opt. Express* **19**(15), 13839–13847 (2011).
47. E. Sapoznik, B.-J. Chang, and J. Huh, "A versatile oblique plane microscope for large-scale and high-resolution imaging of subcellular dynamics," *eLife* **9**, e57681 (2020).
48. F. Stehr, J. Stein, and F. Schueder, "Flat-top tirf illumination boosts dna-paint imaging and quantification," *Nat. Commun.* **10**(1), 1268 (2019).
49. H. Shroff, C. Galbraith, and J. Galbraith, "Live-cell photoactivated localization microscopy of nanoscale adhesion dynamics," *Nat. Methods* **5**(5), 417–423 (2008).
50. F. Gao and L. Han, "Implementing the nelder-mead simplex algorithm with adaptive parameters," *Comput. Optim. Appl.* **51**(1), 259–277 (2012).
51. J. Ries, "SMAP: a modular super-resolution microscopy analysis platform for SMLM data," *Nat. Methods* **17**(9), 870–872 (2020).
52. Y. Wang, J. Schnitzbauer, Z. Hu, X. Li, Y. Cheng, Z.-L. Huang, and B. Huang, "Localization events-based sample drift correction for localization microscopy with redundant cross-correlation algorithm," *Opt. Express* **22**(13), 15982–15991 (2014).
53. M. Booth, T. Wilson, H.-B. Sun, T. Ota, and S. Kawata, "Methods for the characterization of deformable membrane mirrors," *Appl. Opt.* **44**(24), 5131–5139 (2005).
54. P. Pozzi, C. Smith, E. Carroll, D. Wilding, O. Soloviev, M. Booth, G. Vdovin, and M. Verhaegen, "Anisoplanatic adaptive optics in parallelized laser scanning microscopy," *Opt. Express* **28**(10), 14222–14236 (2020).
55. J. Antonello, J. Wang, C. He, M. Phillips, and M. Booth, "Interferometric calibration of a deformable mirror," Zenodo (2020).
56. V. Patlan, O. Soloviev, and G. V. Vdovin, "Optimal diffraction-limited focusing through static aberrations," *Proc. SPIE* **9194**, 91940E (2014).
57. D. Bertsimas and S. Vempala, "Solving convex programs by random walks," *J. ACM* **51**(4), 540–556 (2004).
58. N. A. K. H. Marijn E. Siemons, M. H. P. Kole, and L. C. Kapitein, "Robust adaptive optics for localization microscopy deep in complex tissue," *Nat. Commun.* **12**(1), 3407 (2021).
59. M. Siemons, B. M. C. Cloin, D. M. Salas, W. Nijenhuis, E. A. Katrukha, and L. C. Kapitein, "Comparing strategies for deep astigmatism-based single-molecule localization microscopy," *Biomed. Opt. Express* **11**(2), 735–751 (2020).
60. C. H. Weng, J. Tang, and K. Y. Han, "Optimizing the performance of multiline-scanning confocal microscopy," *J. Phys. D: Appl. Phys.* **54**(10), 105401 (2021).